

直线超声电机 LLCC 谐振网络设计与参数优化方法*

郭鹏涛¹, 李响¹, 周利锋², 姚志远³

(1. 合肥工业大学电气与自动化工程学院 合肥, 230009)

(2. 南京工程学院工业中心/创新创业学院 南京, 211167) (3. 南京航空航天大学航空学院 南京, 210016)

摘要 针对直线超声电机参数时变性以及驱动电压谐波影响其运行稳定性的问题,通过设计两电感-两电容(简称 LLCC)谐振网络拓扑及优化其输出电压总谐波畸变率(total harmonic distortion, 简称 THD)的方法,提升了电机运行稳定性。首先,采用考虑定/动子接触状态下的等效电路模型,推导出 LLCC 阻抗匹配的计算公式,引入补偿电容改善阻抗匹配的弹性裕度与稳定性;其次,探讨了谐振点附近的 LLCC 匹配电路滤波特性,推导出输出电压 THD 与 LLCC 谐振电路参数的数学关系,分析了变压器寄生参数对 LLCC 谐振电路的影响,并提出以正弦输出电压 THD 值为主要指标的 LLCC 谐振电路优化设计方法;最后,设计了 V 型直线超声电机的 LLCC 谐振驱动器。实验结果表明:谐振网络中串、并联电容的比值决定输出电压幅值增益水平、THD 和串联电容两端电压峰值,且前两者相互制衡;并联电感值为软开关特性的主要决定因素;驱动电压 THD 值控制在 3% 以内,相比优化前提升了 70% 以上。

关键词 直线超声电机;LLCC 谐振网络;阻抗匹配;谐波抑制

中图分类号 TH113;TM359

引言

直线超声电机(linear ultrasonic motor, 简称 LUM)为新型微特直线电机,其利用压电陶瓷的逆压电效应激发出定子的超声频机械共振,进而在定子驱动足处产生微观椭圆运动,通过定动子的摩擦传动机制转换为动子的宏观直线运动^[1-2]。与传统电磁电机相比,直线超声电机具有结构简单、功率密度高、响应快、抗电磁干扰能力强及可直接驱动负载等优点,在航天器、精密定位平台及微型机器人等领域具有重要的应用前景^[3-5]。

超声电机虽具有上述优点,但其内部机械阻抗有很强的非线性和时变特性,在定动子接触过程中随边界条件、温度等因素变化发生较大改变^[6-9]。此外,超声电机所需驱动电压大多由低压直流电(DC12~24 V)逆变为高压(AC100~200 V)方波,经滤波网络输出高压正弦波。驱动电压的峰值、相移及 THD 等均对电机运行效果有很大影响^[10-11],这就要求驱动电路充分考虑在动态边界条件下的阻抗匹配问题,得到幅值和相位不随负载(电机)阻抗的变化而变化的输出电压,同时具有良好的 THD,以实现电机的最优驱动效果。

一般由 2 个谐振电感和 2 个谐振电容经不同的组合方式组成的 4 阶谐振电路,统称为 LLCC 谐振滤波器。傅平^[12]应用 LLCC 谐振匹配,实现了输出两相高频正弦电压来驱动超声电机。Lin 等^[13]将 LLCC 匹配网络应用在模糊控制中,设计出电压、相移稳定性较高的自适应控制系统。卢其威等^[14]基于移相全桥逆变拓扑结构,建立功率器件的损耗模型,实现固定频率下低损耗、低 THD 的大功率正弦逆变输出。Zhang 等^[15]利用 LLCC 匹配实现了低温漂驱动电源。Li 等^[16]提出一种用于驱动超声高功率压电致动器的新型逆变器,减少电机电压的总谐波失真,并局部补偿压电致动器的无功功率。Shafiei 等^[17]利用 LCLC 谐振匹配实现了高压软开关输出,提高了逆变器的效率。俞浦等^[18]设计的旋转超声电机的 LLCC 匹配网络,满足电压幅值和相角不随负载和驱动频率变化而改变,仅以主电路实现软开关、电压幅值和相移为目标。如果来实现电机的高性能驱动,必须考虑高次谐波对其非目标振动模式的影响,且因为构成特定频率范围内 LLCC 谐振网络的电容、电感选取有多种方案,还需进一步分析各元件参数的限制条件与最佳匹配组合。

针对上述问题,笔者采用接触状态下的直线超

* 国家自然科学基金资助项目(52105092,52075261)

收稿日期:2023-08-22;修回日期:2023-10-07

声电机定子等效电路^[19],以稳定幅值和相移为基本限制条件,以低THD的输出电压为优化目标,对超声电机的LLCC阻抗匹配网络进行分析。

1 主电路分析

单相LLCC谐振电路如图1所示。其中,半桥逆变电路由电力场效应管与高频变压器组成,匹配电路由外加无源电感 L_r 、 L_s 及无源电容 C_s 、 C_c 组成。电机的等效电路由电气支路、机械支路和接触支路组成,其中压电陶瓷的静态电容 C_d 构成电气支路。在定动子未接触状态下,电机质量效应的等效电感 L_{m0} 、弹性效应的等效电容 C_{m0} 、定子内机械损耗的等效电阻 R_{m0} 串联构成动态机械支路,其决定电机机电耦合特性;在定动子接触状态下,电阻 R_f 等效为定动子在摩擦传动过程中的能量损耗,电容 C_f 等效为定子传递至动子的能量。

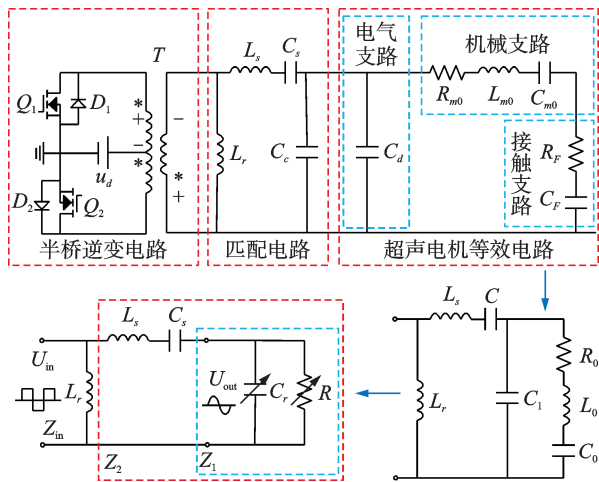


图1 单相LLCC谐振电路

Fig.1 Single-phase LLCC resonant circuit

电机的等效电路参数受边界条件的改变而动态变化,所以在静态电容两端并联补偿电容 C_c ,以降低因夹持电容在运行过程中的变化对匹配电路干扰的权重,同时也使LLCC匹配电路的参数选择弹性化。

将推挽变压器 T 视为理想变压器,可把图1上方的匹配电路和超声电机等效电路分两步简化为如图1左下方电路,其中: L_s 、 C_s 为串联匹配电感和电容; L_r 、 C_c 为并联电感和电容,其共同组成LLCC谐振阻抗匹配网络。简化后的等效电容 C_r 和电阻 R 也具有时变特性,随电机不同的边界条件呈非线性变化。各参数变换关系为

$$\begin{cases} L = L_0 - 1/(\omega^2 C_0) \\ R = R_0 + (\omega L)^2 / R_0 \\ C_r = C_1 - L / [(\omega L)^2 + R_0^2] \\ C_1 = C_c + C_d \end{cases} \quad (1)$$

其中: L 为过渡变量; C_c 为补偿电容。

谐振网络电压增益及其相位为

$$G = \frac{Z_1}{Z_2} = \frac{1}{\left(1 + \frac{C_r}{C_s} - \omega^2 L_s C_r\right) + j\left(\frac{\omega L_s}{R} - \frac{1}{\omega R C_s}\right)} \quad (2)$$

$$\angle G = \arctan \frac{\omega L_s / R - 1 / \omega R C_s}{1 + C_r / C_s - \omega^2 L_s C_r} \quad (3)$$

其中: Z_1 为超声电机与补偿电容 C_c 的总阻抗; Z_2 为变压器副边侧除 L_r 的阻抗。

当式(2)分母虚部为0、实部为1时,电压增益为1,此时谐振网络的相位 $\angle G = 0$,在谐振频率附近有

$$\omega L_s - 1 / \omega C_s = 0 \quad (4)$$

谐振网络与超声电机的总阻抗为

$$Z = \frac{\omega L_r [\omega R (\omega^2 L_s C_s C_r - C_r - C_s) + j(1 - \omega^2 L_s C_s)]}{1 - \omega^2 C_s (L_r + L_s) + j\omega R [C_r + C_s - \omega^2 C_r C_s (L_r + L_s)]} \quad (5)$$

由式(4)可知,在谐振频率附近, Z 的分子虚部近似为0,若使总阻抗为阻性,仅需分母虚部为0,即

$$\omega L_r - 1 / \omega C_r = 0 \quad (6)$$

本次仿真及实验所用电机为一款自研的额定功率为12W的V型直线超声电机,利用阻抗分析仪可对考虑定、动子接触的定子等效电路进行参数识别^[19]。识别后的V型直线超声电机参数见表1,其中施加给定子的预压力为80N。

表1 V型直线超声电机参数

Tab.1 Parameters of V-shaped linear ultrasonic motor

参数	A相	B相
R_0/Ω	636.775	411.229
L_0/mH	365.658	293.248
C_0/pF	44.519	55.872
C_d/nF	2.075	2.001
f_r/kHz	39.447	39.319

2 LLCC电路的滤波特性分析

匹配电路输入电压与基波电压如图2所示。其中:实线部分为推挽逆变电路输入至匹配电路的方波电压 u_m ;虚线部分为基波分量 u_{m1} 。对 u_m 进行傅里

叶分析,得到

$$u_{in}(t) = \frac{4U}{n\pi} \sum_{n=1,3,5\dots}^{\infty} \sin(n\omega t) \quad (7)$$

$u_{in}(t)$ 包含了3,5,7,⋯等高次谐波成分,会激发压电陶瓷组的非目标振动模态,影响电机运行效果。同时,仅满足式(4)和式(6)的 L_r 、 L_s 、 C_r 及 C_s 有无数种组合,因此需要研究这些元件在不同取值时对输出电压的影响及其选型的限制条件。

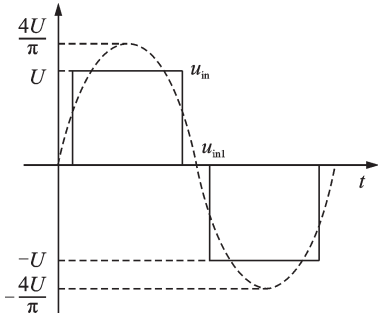


图2 匹配电路输入电压与基波电压

Fig.2 Input and fundamental voltages of matching circuit

\dot{u}_{out} 和 \dot{u}_{in} 分别为匹配电路输出正弦电压和输入方波电压的向量表示,其关系为

$$G(j\omega) = \dot{u}_{out} / \dot{u}_{in} = Z_1 / Z = \frac{\omega R^2(C_s + C_r - C_r A) + jR(A - 1)}{(B + \omega^2 R^2 C_r C) + j\omega R(C_r B - C)} \quad (8)$$

其中: $A = \omega^2 C_s(L_s + L_r)$; $B = \omega L_r(1 - \omega^2 L_s C_s)$; $C =$

$$THD_{u_{out}} = \frac{\sqrt{\sum_{n=3,5\dots} |u_{out}(n)|^2}}{|u_{out}(L)|} = \sqrt{\sum_{n=3,5\dots} \left| \frac{a + 1 + j \left[\frac{aQ_s}{n(1-n^2)} (n^3 a - 1) \right]}{n^2 \left[a^2 Q_s^2 - \frac{n^2(a+1-n^2)}{1-n^2} \right] + jn^3 a Q_s \left[2 + \frac{a}{(1-n^2)} \right]} \right|^2} \quad (12)$$

由式(11)可以看出,各次谐波输出幅值大小与 a 、品质因数 Q_s 有关。根据式(12),利用Matlab绘出 a 、 Q_s 与高次谐波含量的三维关系曲线, a 和 Q_s 对THD的影响如图3所示。可以看出,9次及以上谐波含量占总THD含量不足0.1%,因此本研究中THD计算仅考虑抑制3,5,7次谐波。

选取不同的 a 和 L_s 代入式(9),分别得到 L_r 、 C_r 和 C_s 。根据式(2)、式(3)得到 L_s 与输出电压增益和相移的关系,如图4所示。可以看出:输出电压增益会随着频率的增大而线性增大,随着 a 减小,将造成电压增益在驱动频域内的幅值波动增大;输出电压的相移主要由 L_s 决定,在谐振频率附近波动相对剧烈,但总体仍处于较低水平。因此,为了使输出电压增益、相移在不同频段变化尽量小,一般选择 $a > 0.3$

$\omega L_r(\omega^2 L_s C_r C_s - C_r - C_s)$ 。

为了分析LLCC谐振电路在谐振频率 ω_r 附近的滤波特性,定义

$$\begin{cases} Q_s = \omega_r L_s / R = 1 / \omega_r C_s R \\ Q_p = R / \omega_r L_r = \omega_r C_r R \\ a = 1 / Q_s Q_p = L_r / L_s = C_s / C_r \\ n = \omega / \omega_r \end{cases} \quad (9)$$

其中: Q_s 为品质因数。

将式(9)代入式(8),可得

$$G(jn\omega_r) = \frac{(1-n^2)(a+1) + j \left[\frac{aQ_s}{n} (n^3 a - 1) \right]}{[(1-n^2)a^2 Q_s^2 - n^2(a+1-n^2)] + jnaQ_s[2(1-n^2)+a]} \quad (10)$$

将式(10)乘以式(7)中的各次谐波电压的幅值,可以得到

$$\dot{U}_{out}(n) = u_{in(n)} G(jn\omega_r) = \frac{4U}{n\pi} \sin\left(\frac{n\pi}{2}\right) \times \frac{(1-n^2)(a+1) + j \left[\frac{aQ_s}{n} (n^3 a - 1) \right]}{[(1-n^2)a^2 Q_s^2 - n^2(a+1-n^2)] + jnaQ_s[2(1-n^2)+a]} \quad (11)$$

其中: $\dot{U}_{out}(n)$ 为输出电压的各次谐波。

$\dot{U}_{out}(n)$ 的波形畸变率 $THD_{u_{out}}$ 可表示为

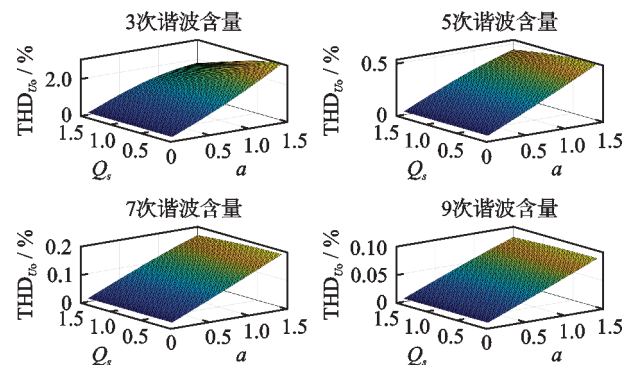


图3 a和 Q_s 对THD的影响

Fig.3 The impact of a and Q_s on THD

和 $L_s < 5$ mH。由于装配工艺问题,超声电机的两相参数不完全相同,可大致取两相机械谐振频率的中间值 $f_r = 39.4$ kHz为参考谐振频率,也作为进行LLCC匹配的目标频率和电机初始驱动频率。

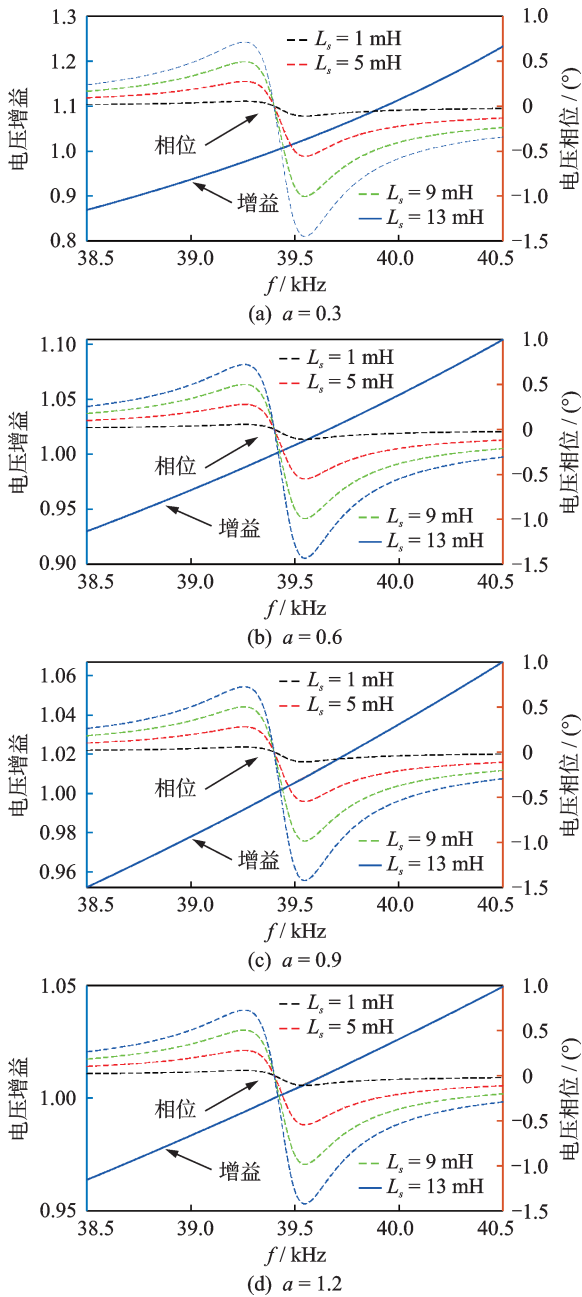


图4 L_s 与输出电压增益和相位的关系

Fig.4 The relationship between L_s and the gain and phase of the output voltage

考虑到超声电机可以调频调速,且运行过程中会发生频率漂移现象,需闭环频率跟踪,因而要对不同频率匹配电路输出性能进行分析。根据式(1)、式(4)、式(6)及表1,在 f_r 附近频率下对LLCC匹配电路进行Matlab/Simulink仿真分析,得到频率和串联电感的关系。A相定子匹配仿真如表2所示。由表可知,当 a 确定时,不同驱动频率下THD均随 L_s 的增大而线性增大。由于 Q_s 的大小随频率波动较大,不能以不同频段的 Q_s 来进行匹配电路的选型,故仅对 f_r 下的 Q_s 进行分析。

表2 A相定子匹配仿真($a=0.5$)

Tab.2 Simulation of A-phase stator matching($a=0.5$)

f/kHz	L_s/mH	THD/%	Q_s
39.0	1	2.571	0.033
	5	3.552	0.167
	8	4.959	0.267
39.3	1	2.485	0.181
	5	3.432	0.907
	8	4.827	1.632
39.5	1	2.425	0.341
	5	3.366	1.705
	8	4.686	2.728
39.8	1	2.274	0.053
	5	3.185	0.265
	8	4.490	0.424

选取不同 a 与 Q_s 进行Matlab/Simulink仿真,得到不同 Q_s 时的THD与 a 的关系曲线,如图5所示。不同 a 时的THD、电容 C_s 的端电压与 Q_s 的关系曲线如图6所示。与图3相比,图5、图6的仿真结果进一步验证了 Q_s 的变化对于LLCC匹配电路输出电压的THD影响很小,且随着 Q_s 的增大,THD呈减小趋势。对比图4与图6发现, a 增大会造成输出电压总谐波畸变率的线性增大,但也会使增益曲线的斜率减小,两者相互制衡,在实际电源制作过程中需根据目标电机的特点综合考虑选取。由图6还可看出,串联谐振电容 C_s 上的电压会随着 a 的减小而近似线性增大,因此需要先确定 a ,再根据峰值上限与安全裕度选取滤波电容 C_s 的型号。

为避免补偿电容 C_c 为负数,应满足

$$C_{r\min} - C_d = \frac{1}{4a\pi^2 L_s f_{\max}^2} - C_d > 0 \quad (13)$$

其中: $C_{r\min}$ 为最小并联电容; f_{\max} 为最大驱动频率。

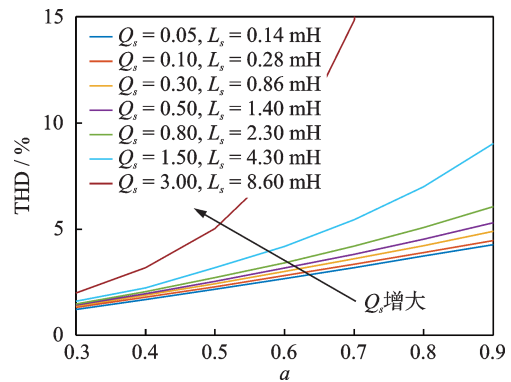


图5 取不同 Q_s 时的THD与 a 的关系曲线

Fig.5 The relationship curve between THD and a when taking different values of Q_s

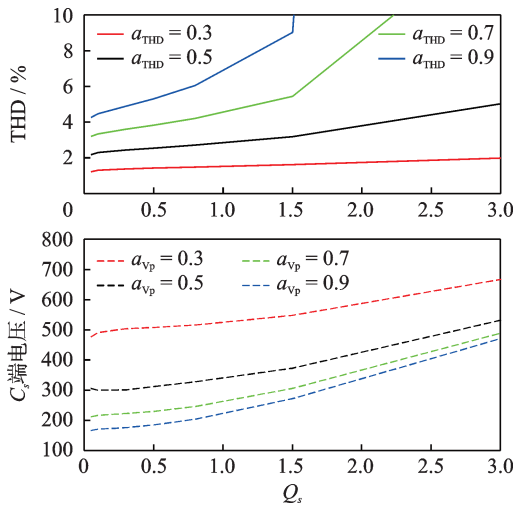


图 6 取不同 α 时的 THD、电容 C_s 的端电压与 Q_s 的关系曲线
Fig.6 The relationship curve between the voltage of THD, capacitor C_s and Q_s when taking different values of α

3 推挽变压器对 LLCC 电路的影响

变压器等效及其简化电路如图 7 所示。图 7(a) 中: $L_{m1,2}$ 、 $C_{1,2}'$ 、 $L_{1,2}$ 和 $R_{1,2}'$ 分别为变压器原边两绕组的励磁电感、匝间电容、漏感和串并联等效电阻; L_{m3} 、 L_3 分别为变压器副边的励磁电感和漏感。推挽变压器一般采用多股导线并绕的方式,原边 2 个绕组的对应参数大致相等。由于电路负载阻抗相对较大,因此实际变压器的寄生参数 $C_{1,2}' \approx 0$,且 $R_{1,2}'$ 远小于电机电阻,即 $C_{1,2}'$ 和 $R_{1,2}'$ 对输出电压的影响可以忽略不计,图 7(a) 可简化为图 7(b)。图 7(b) 中的 $L_{m1,2}$ 对开关管零电压导通有积极影响,但会严重降低输出电压幅值和引起尖峰电压。综合考虑下,笔者没有利用原边漏感实现软开关,所以在制作变压器时尽可能使原边漏感与励磁电达到最小。同时,实际测量的 $\omega L_{1,2}$ 远小于超声电机等效电阻,其对于理论计算影响很小。

根据式 (4) 和式 (6) 可将变压器副边侧整体匹配为阻性,使开关管处于损耗较大硬开关状态,且驱动频率在一定范围内调整,整体电路阻抗性质时变性

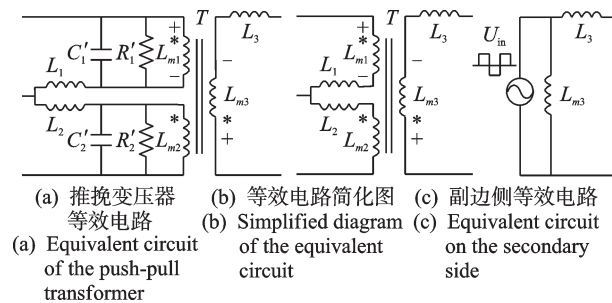


图 7 变压器等效及其简化电路

Fig.7 Equivalent and simplified circuit of transformer

大。工作在感性负载相较于容性负载工况下可以实现软开关零电压开通,且能够避免容性负载下出现几倍于正常电流的开关尖峰电流^[20]。在确定匹配电路中的各参数后,由式(8)得到 L_r 与总阻抗 Z 的相位关系,如图 8 所示。由图可知,若要满足在驱动频率带宽内系统总阻抗为感性状态,则需要式(6)的基础上进一步结合图 8 对 L_r 重新选型。在本研究中,当 $L_r < 3$ mH 时总阻抗呈感性,为了避免 L_r 消耗过多的无功电流,一般将其选择为略小于临界电感,使总阻抗在谐振频率处呈弱感性即可。

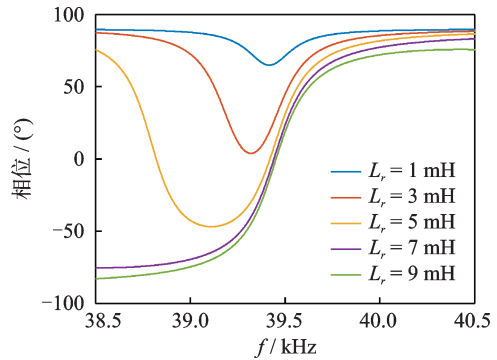


图 8 L_r 与总阻抗 Z 的相位关系

Fig.8 Phase relationship between L_r and total impedance Z

从电压的角度看,变压器副边侧可以视为高压方波与副边励磁电感 L_{m3} 并联,再与副边漏感 L_3 串联,如图 7(c) 所示。此时,最理想的匹配状态是 L_3 完全代替 LLCC 匹配电路的串联谐振电感 L_r , L_{m3} 完全代替 L_r ,这样可以减小电路元件数量和电路体积。本实验通过改变绕组线圈相对位置设计推挽变压器的副边漏感,改变各绕组的气隙设计推挽变压器的励磁电感。

4 设计步骤和实验验证

当设计超声电机电源时,应当从提高输出电压幅值和相移稳定性、减小输出电压 THD、提高电源效率及减小元器件过大的电压电流应力方面综合考虑,其中 α 的大小对增益脉动、总谐波畸变率和串联谐振电容 C_s 上的电压有着关键影响。LLCC 匹配电路设计步骤如图 9 所示。笔者基于此方法,针对 V 型直线超声电机设计了输出 $f = 39.4$ kHz 和 $THD < 3\%$ 的正弦波、功率为 15 W 的驱动电源。设计参数与计算参数如表 3 所示。

基于 ARM 控制器的 V 型直线超声电机驱动实验平台见图 10。其中:可编程直流电源用于提供驱动电路的能量;示波器用于测量电机输入电压(匹配电路输出电压)与开关管漏源极电流;电流探头用于

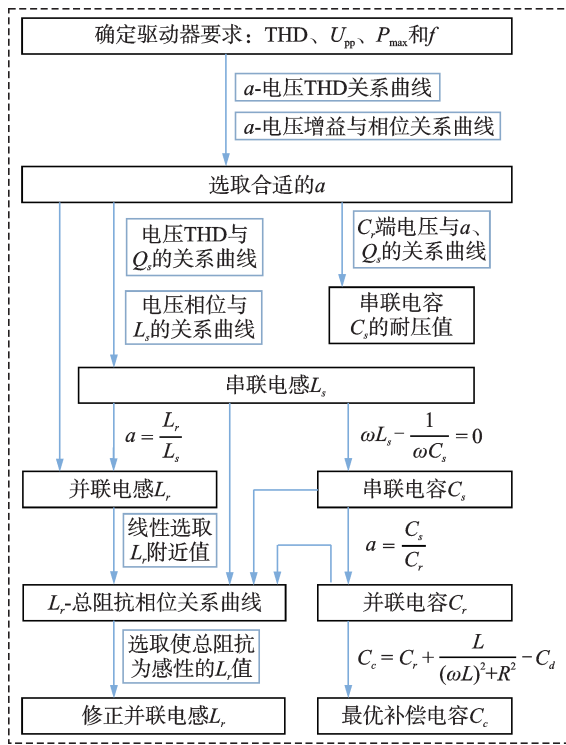


图9 LLCC匹配电路设计步骤
Fig.9 LLCC matching circuit design steps

表3 设计参数与计算参数

设计参数	数值	计算参数	数值
U_{dc}/V	12	L_s/mH	3.000
P_o/W	15	C_s/nF	5.440
k	10:1	$L_r=L_{m3}/mH$	2.000
f/kHz	38.5~40.5	C_{cA}/nF	6.850
a	0.5	C_{cB}/nF	13.520
f_r/kHz	39.4	Q_{sA}	1.043
THD/%	<3	Q_{sB}	1.195

U_{dc} 为直流输入电源电压; k 为推挽变压器变比

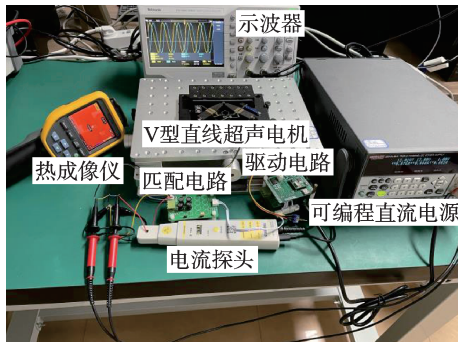
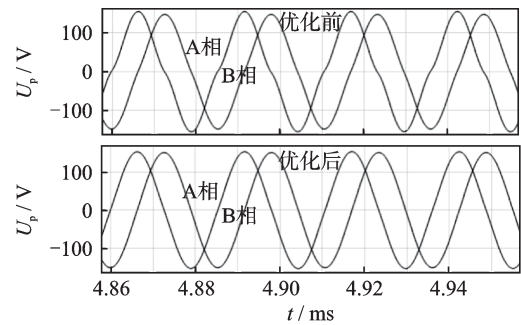


图10 基于ARM的V型直线超声电机驱动实验平台
Fig.10 ARM based experimental platform for driving V-shaped linear ultrasonic motor

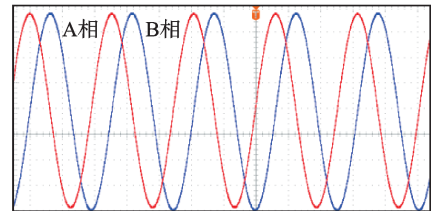
辅助示波器测量开关管漏源极电流;热成像仪用于测量匹配至感性与容性条件下的开关管温升图。

两相电压输出及THD分析如图11所示。图11(a)为 $f_r=39.4\text{ kHz}$ 时带载的两相输出电压经LLCC匹配前后仿真波形,可以看出,仅考虑增益和相移等因素的优化前仿真波形已出现明显的正弦波形的畸变。图11(b)为匹配后实际输出的波形,与输入方波的基波幅值 152.793 V 及 90° 的目标相位差偏差较小,偏差主要来源于:①两相定子参数不完全相同;②温度上升导致谐振频率值下降;③示波器在大尺度下显示不精准。图11(c)为仿真与实际输出波形的THD对比,可以发现,LLCC匹配经优化后高次谐波得到大幅度抑制,由于电机在运行过程中温度上升,导致静态电容 C_d 的容值增大,进而 a 小幅度减小,这可能是实际输出电压低于仿真输出电压的THD水平的主要原因。

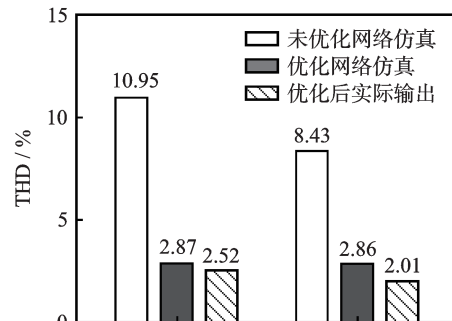
不同频率下输出电压的理论值与测量值如图12所示。电压增益会随着频率的增加出现小幅



(a) LLCC匹配优化前、后仿真波形
(a) LLCC matching before and after optimization to output simulation waveforms



(b) LLCC匹配优化后实际输出波形
(b) Output waveform after LLCC matching optimization



(c) THD结果对比分析
(c) Comparative analysis of THD results

图11 两相电压输出及THD分析

Fig.11 Voltage output and THD analysis of two phases

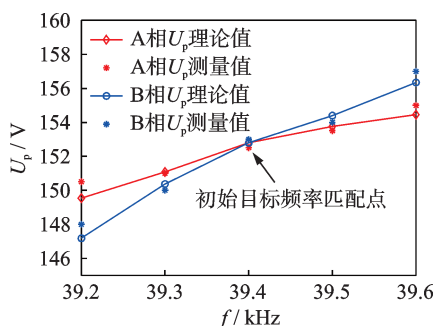


图 12 不同频率下输出电压的理论值与测量值

Fig.12 Theoretical and measured values of output voltage at different frequencies

度上升趋势,因为实际的超声电机精密控制下的驱动频率漂移一般在谐振点附近 100~200 Hz 左右,所以施加在电机上的峰值电压最大偏移仅为 $\pm 1\sim 4$ V,实际产生的位移误差很小,并很容易通过算法实现补偿。在同等条件下,使用 LC、LLCC 匹配对电机分别进行堵转测试,前者堵转力为 13.5 N,后者为 21.9 N,堵转力提升了 62.2%。

开关管漏极电流 i_{ds} 和漏源极电压 u_{ds} 实测波形如图 13 所示。可以看到:开关管导通前其反向并联二极管先导通,将开关管漏源极两端电压箝位为 0,当续流过程结束后,开关管漏源极电流从 0 线性增加,成功实现零电压导通;当开关管关断时,原边电流给开关管结电容充电,漏源极电压从 0 开始增加,关断过程中在漏源极内部并未同时产生较大的电压电流汇聚,仅有相对很小的能量损耗。在图 13 中 i_{ds} 左右两侧,开关管漏极电流在开关瞬间都没有出现尖峰电流,相对容性负载大大减小了开关损耗和器件应力,提高了驱动效率和可靠性。

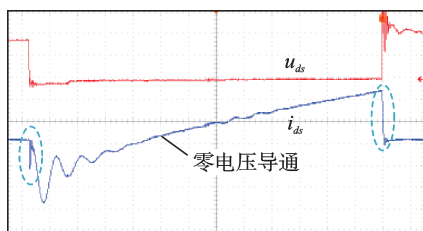


图 13 i_{ds} 和 u_{ds} 实测波形

Fig.13 The measured waveforms of i_{ds} and u_{ds}

感性与容性负载开关管温升实验对比如图 14 所示。可以看到,在室温为 22 °C 条件下,感性负载相较于容性负载的开关管有明显的温度下降,进一步验证了感性负载下开关管损耗较小。从图 14(b) 可以发现,由于容性负载存在尖峰电流,在电源输入端口出现严重发热,会对周围器件产生不良影响,降低了电源稳定性,且不利于驱动器的小型化。

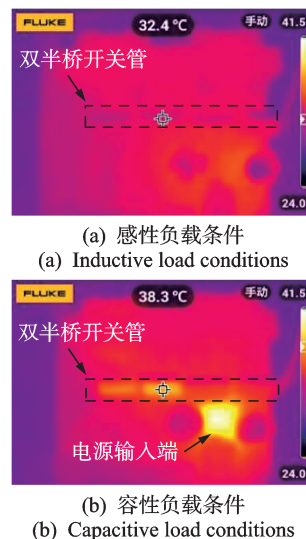


图 14 感性与容性负载开关管温升实验对比图

Fig.14 Comparison of temperature rise between inductive and capacitive load switch tubes

5 结 论

1) 采用推挽拓扑电路,考虑基于定、转子接触的直线超声电机定子等效电路,得到 LLCC 谐振匹配拓扑并加以简化。根据简化模型,推导出 LLCC 参数与输出电压幅值和相移的代数关系,并以此作为 THD 优化的基本限制条件。

2) 对 LLCC 谐振匹配进行理论分析,发现串联电容与并联电容的比值对输出电压幅值的增益、THD 和串联电容两端电压峰值大小起决定性作用,且为相互制衡关系;并联电感的值为软开关和输出电压相移的主要决定因素。结合变压器对 LLCC 网络进行优化设计,给出了带补偿电容的谐振网络参数设计方法。

3) 设计了一款用于直线超声电机的 V 型 LLCC 谐振驱动器,并进行了参数优化。将驱动电压 THD 值控制在 3% 以内,比未经优化的 LLCC 匹配提升了 70% 以上,且相对于传统的 LC 谐振匹配电路,电机堵转力提升了 60% 以上,对直线超声电机驱动器的谐振匹配电路设计与优化具有参考价值。

参 考 文 献

[1] 李晓牛. V 形直线超声电机动力学建模与应用研究 [D]. 南京: 南京航空航天大学, 2017.

[2] LI X, GUO P T, DING Y, et al. A generalized electromechanical coupled model of standing-wave linear ultrasonic motors and its nonlinear version [J]. Mechanical Systems and Signal Processing, 2023, 186: 109870.

- [3] 姚志远, 李晓牛, 李响, 等. 直线超声电机设计, 建模和应用的研究进展[J]. 振动、测试与诊断, 2016, 36(4): 615-623.
YAO Zhiyuan, LI Xiaoni, LI Xiang, et al. Research progress on the design, modeling, and application of linear ultrasonic motors [J]. Journal of Vibration, Measurement & Diagnosis, 2016, 36(4): 615-623. (in Chinese)
- [4] 刘英想, 邓杰, 常庆兵, 等. 压电驱动技术研究进展与展望[J]. 振动、测试与诊断, 2022, 42(6): 1045-1061.
LIU Yingxiang, DENG Jie, CHANG Qingbing, et al. Research progress and prospects of piezoelectric drive technology [J]. Journal of Vibration, Measurement & Diagnosis, 2022, 42(6): 1045-1061. (in Chinese)
- [5] 赵淳生. 超声电机技术与应用[M]. 北京: 科学出版社, 2007: 1-2.
- [6] NAKAGAWA Y, SAITO A, MAENO T. Nonlinear dynamic analysis of traveling wave-Type ultrasonic motors[J]. IEEE Transactions on Ultrasonics, Ferroelectrics, and Frequency Control, 2008, 55(3): 717-725.
- [7] LU X L, HU J H, ZHAO C S. Analyses of the temperature field of traveling-wave rotary ultrasonic motors[J]. IEEE Transactions on Ultrasonics, Ferroelectrics, and Frequency Control, 2011, 58(12): 2708-2719.
- [8] 荆锴, 林夏萍, 王婕, 等. 行波超声电机振动模式非线性滑模观测器与协调控制[J]. 电机与控制学报, 2021, 25(4): 72-80.
JING Kai, LIN Xiaping, WANG Jie, et al. Nonlinear sliding-mode observer of travelling-wave ultrasonic motor vibration modes and coordination control [J]. Electric Machines and Control, 2021, 25(4): 72-80. (in Chinese)
- [9] QI X, SHI W J, WANG S K, et al. Compensating nonlinear temperature dependence of ultrasonic motor [J]. Ultrasonics, 2021, 117: 106522.
- [10] LI X N, HUANG T L, ZHAO N, et al. A design method of traveling wave rotary ultrasonic motors driving circuit under high voltage using single-sided hertzian contact forced oscillator model [J]. Micromachines, 2023, 14(64): 1-15.
- [11] 陈宁. 超声电机驱动特性与高精度测控方法研究[D]. 长沙: 国防科技大学, 2020.
- [12] 傅平. 超声波电机的LLCC驱动电路分析[J]. 重庆大学学报, 2014, 37(7): 11-19.
FU Ping. Analysis of LLCC resonant driving circuit for ultrasonic motor [J]. Journal of Chongqing University, 2014, 37(7): 11-19. (in Chinese)
- [13] LIN F J, WAI R J, LIN H H. An adaptive fuzzy-neural-network controller for ultrasonic motor drive using the LLCC resonant technique [J]. IEEE Transactions on Ultrasonics, Ferroelectrics, and Frequency Control, 1999, 46(3): 715-727.
- [14] 卢其威, 邓欢, 陈婷, 等. LLCC谐振滤波器在高频正弦波逆变器中的优化设计[J]. 电工技术学报, 2017, 32(20): 142-152.
LU Qiwei, DENG Huan, CHEN Ting, et al. Parameters optimization and design of LLCC resonant converter in high frequency sinusoidal inverter [J]. Transactions of China Electrotechnical Society, 2017, 32(20): 142-152. (in Chinese)
- [15] ZHANG Z F, CHEN W Z, WAI R J. Design of high step-up driving circuit for linear ultrasonic motor [C] // 2017 International Conference on Applied System Innovation. Sapporo, Japan: IEEE, 2017: 1347-1350.
- [16] LI R Y, FROHLEKE N, BOCKER J. LLCC-PWM inverter for driving high-power piezoelectric actuators [C] // 2008 13th International Power Electronics and Motion Control Conference. Poznan, Poland: IEEE, 2008: 159-164.
- [17] SHAFIEI N, PAHLEVANINEZHAD M, FARZANEHFARD H, et al. Analysis and implementation of a fixed-frequency LCLC resonant converter with capacitive output filter [J]. IEEE Transactions on Industrial Electronics, 2011, 58(10): 4773-4782.
- [18] 俞浦, 李华峰, 黄卫清. 超声电机LLCC谐振电路研究[J]. 中国电机工程学报, 2011, 31(24): 105-110.
YU Pu, LI Huafeng, HUANG Weiqing. Research on LLCC resonant circuit of ultrasonic motor [J]. Proceedings of the CSEE, 2011, 31(24): 105-110. (in Chinese)
- [19] GUO P T, DING Y, LI X, et al. Equivalent circuit modeling for V-shape linear ultrasonic motor [C] // 2022 16th Symposium on Piezoelectricity, Acoustic Waves, and Device Applications (SPAWDA). Nanjing: IEEE, 2022: 214-218.
- [20] 颜佳佳, 阮新波, 李华峰, 等. 超声电机的软开关驱动电路[J]. 中国电机工程学报, 2009, 29(3): 109-114.
YAN Jiajia, RUAN Xinbo, LI Huafeng, et al. Soft switching driving circuit for ultrasonic motor [J]. Proceedings of the CSEE, 2009, 29(3): 109-114. (in Chinese)



第一作者简介:郭鹏涛,男,1999年5月生,硕士生。主要研究方向为超声电机驱动技术。曾发表《A generalized electromechanical coupled model of standing-wave linear ultrasonic motors and its nonlinear version》(《Mechanical Systems and Signal Processing》2023, Vol.186)等论文。

E-mail: A15690864573@163.com

通信作者简介:李响,男,1986年12月生,博士、副教授。主要研究方向为超声电机动力学建模与驱动控制技术。

E-mail: lixiang@hfut.edu.cn

obtained through experiments under various acceleration amplitude conditions, and a smooth simple harmonic force surface is constructed using linear interpolation. Then, by extracting the contour lines corresponding to constant force amplitude from this surface, the frequency response curve of the nonlinear structure under constant-force conditions is derived. Finally, the dynamic characteristics of a typical bolted nonlinear structure are investigated. The results show that the proposed approach can accurately capture the frequency response characteristics of bolted nonlinear structures, revealing the pronounced nonlinear dependence on force amplitude. Furthermore, bolt preload and structural reassembly are found to significantly influence the dynamic characteristics of the connection structure.

Keywords nonlinear structure ; response-controlled; dynamics characteristic; harmonic force surface; experimental technology

Mechanical Fault Diagnosis of In-wheel Motor Based on Weibull Kernel Function and MCSVDD

LIU Bingchen, XUE Hongtao, DING Dianyong

(School of Automotive and Traffic Engineering, Jiangsu University Zhenjiang, 212013, China)

Abstract In order to monitor the operation state of each wheel motor in distributed drive electric vehicle and ensure the safety of the vehicle, a fault diagnosis method of in-wheel motor based on improved multi-class support vector data description (MCSVDD) is proposed. The method incorporates two major improvements. First, a classification judgment rule based on the minimum distance to the cluster center within the class is proposed using the affinity propagation (AP) clustering algorithm to enhance MCSVDD. Second, a Weibull kernel function is constructed from the Weibull distribution to optimize data description model. Meanwhile, a dimensionality reduction method based on minimum-distance propagation discriminant projection (MPDP) is proposed for the multi-dimensional feature set of in-wheel motor operating state, which improves the separability of in-wheel motor fault states under different working conditions. Finally, in-wheel motors with typical bearing faults are customized respectively to collect vibration signals under 7 rotating speeds for verifying the effectiveness of the proposed method. The results show that the reduced dimension data's separability of observed samples of in-wheel motor operating state based on MPDP is better than that of linear discriminant analysis (LDA), minimum-distance discriminant projection (MDP) and locality preserving projection (LPP), and the recognition accuracy of MCSVDD's state recognition system based on Weibull kernel function is higher than that of polynomial and Gaussian kernel function.

Keywords in-wheel motor; vibration signal; fault diagnosis; minimum-distance propagation discrimination projection; multi-class support vector data description; Weibull kernel function

Design and Parameter Optimization of LLCC Resonant Network for Linear Ultrasonic Motors

GUO Pengtao¹, LI Xiang¹, ZHOU Lifeng², YAO Zhiyuan³

(1. School of Electrical Engineering and Automation, Hefei University of Technology Hefei, 230009, China)

(2. Industrial Center/School of Innovation and Entrepreneurship, Nanjing Institute of Technology Nanjing, 211167, China)

(3. College of Aerospace Engineering, Nanjing University of Aeronautics and Astronautics Nanjing, 210016, China)

Abstract Aiming to address the operation stability affected by the parameter time-variation of the ultrasonic

motor and the harmonic effect of the drive voltage, this paper focuses on the design and optimization of LLCC resonant network topology as well as total harmonic distortion (THD) of the output voltage for driving linear ultrasonic motors (LUMs). Such method can effectively overcome the issue on the variations of the driving voltages caused by the parameter time-variation to improve their operation stability. Firstly, the calculation method for the LLCC matching parameters is derived by using a contact-based equivalent circuit of LUMs considering the stator/mover contact boundary conditions, and a compensation capacitor is added to improve the elasticity margin and the stability of impedance matching. Furthermore, the filtering characteristics of the LLCC resonant network near the resonant frequency is discussed in depth, and the mathematical relationships are derived between the THD of the output voltage and the parameters of the LLCC resonant network are derived. Furthermore, the influence of the parasitic parameters of the transformer on the LLCC resonant network is also analyzed. On this basis, the design optimization methodology for the LLCC resonant network is proposed while acting the THD of the sinusoidal output voltage as the main target. Finally, a LLCC resonant driver is designed for a V-shape LUM, and the corresponding experiments are conducted. The results indicated that the gain and the THD of the output voltage as well as the peak amplitude of the series capacitor voltage itself are determined by the ratio of the series capacitor and the parallel capacitor in the resonant network. The series inductor is the dominating factor for the soft switching characteristics. The THD of the output voltage is controlled below 3%, which is improved more than 70% compared to the unoptimized LLCC resonant driver.

Keywords linear ultrasonic motor; LLCC resonant network; impedance matching; harmonic suppression

Research on Characteristics of Typical Gas Path Fault Components in Aircraft Engines

WANG Jingwei¹, YU Zhuang^{2,3}, YAO Yuan^{2,3}, GENG Jia^{2,3}

(1. Shenyang Engine Research Institute of AVIC Shenyang, 110015, China)

(2. School of Mechanical Engineering, Xi'an Jiaotong University Xi'an, 710049, China)

(3. National Key Lab of Aerospace Power System and Plasma Technology Xi'an, 710049, China)

Abstract In response to unclear mechanisms in compressor fault diagnosis research, this article aims to reveal the variation law of component characteristic changes caused by blade wear, numerical simulation analysis method is used for studying the changes in component characteristics of blades under different degrees of wear. The results show that the degree of compressor performance degradation caused by blade surface wear is more significant than that caused by blade tip wear. With the increased speed, the degree of performance degradation becomes greater. The efficiency decay value caused by the increase of blade tip clearance shows a pattern of first decreasing and then increasing with the increase of pressure ratio. Near the working line of the compressor, the efficiency decay value is relatively stable with the change of pressure ratio, while the flow decay value increases with the increase of pressure ratio. After the increase of blade surface roughness, the decay values of efficiency and flow rate both increase with the increase of pressure ratio. Moreover, there is a decreasing trend in the decay values near stall pressure ratio. Near the working line, varying degrees of blade wear have a greater impact on flow rate than on efficiency. The results can provide a theoretical reference for the research of fault diagnosis methods for aviation engine gas paths.

Keywords air circuit wear failure; tip clearance; blade surface roughness; performance degradation